Combined DRIFTS and DFT Study of CO Adsorption and Segregation Modes in Pt–Sn Nanoalloys

Qing Wang, Didier Tichit, Frédéric Meunier, Hazar Guesmi

Combined DRIFTS and DFT study of CO adsorption and segregation modes in Pt-Sn nanoalloys

Qing Wang[1], Didier Tichit[1], Frederic Meunier[2,*], Hazar Guesmi[1,*]

[1] Institut Charles Gerhardt Montpellier, UM/CNRS/ENSCM, 240, Avenue du Professeur Emile Jeanbrau, 34090 Montpellier, France
[2] Univ Lyon, Université Claude Bernard Lyon 1, CNRS, IRCELYON, 2 Av. Albert Einstein, 69626 Villeurbanne, France.

Abstract

This contribution aims at rationalizing the observations made by *in situ* IR spectroscopy during CO adsorption over 1.8 nm Pt-Sn nanoparticles by Density Functional Theory (DFT) calculations and describing the environment and electronic properties of surface Pt atoms modified by Sn. Pt surface enrichment upon CO exposure was observed by DRIFTS (diffuse reflectance FT-IR spectroscopy) and rationalized by the theoretical calculations, which also indicated that isolated Pt was favored over Pt pairing in a Sn-rich alloy. DFT frequency calculations allowing the fine assignment of vibrational νCO spectra. The results show gradual decay of the linear carbonyl wavenumber from plain Pt (2075 cm^{-1}), through a Sn-poor Pt-Sn (2054 cm^{-1}) and down to a Sn-rich Pt-Sn nanoparticles (2039 cm^{-1}). This decay is accompanied by a weakening of Pt-CO bonds, which confirm the ability of Sn to prevent CO poisoning of Pt when present in a nanoalloy. Moreover, electronic structure analyses evidence a preponderant charge transfer from Sn to Pt atoms, which explains the weakening of both the Pt-CO bond and the C-O bond through back-donation to antibonding molecular orbitals. A weaker C-O bond would favor CO dissociation and the formation of Pt and SnOx ensembles, which is consistent with DRIFTS data recorded at low temperatures.

I. Introduction

Multimetallic catalyst formulations offer clear opportunities in terms of reducing the reliance on noble or rare metals and the improvement of catalyst performances[1–3]. In this context, tin has frequently been used as a promoter to alter the properties of noble metal-based catalysts. For instance, Sn alloyed with Pd, showed significant increase in the selectivity of numerous hydrogenation reactions[4–6]. Choi and Lee reported modifications of the Pd electronic density (so-called ligand effect) and nanoparticle morphologies (so-called geometric or ensemble effect) induced by Sn addition[6]. The reported Pd K-edge XANES data indicated that Sn-free Pd was in an electro-deficient hydride state, while Sn-modified Pd was in a zero valent state and Pd ensembles were replaced with Pd-Sn entities. Using CO adsorption and temperature programmed methods some of us observed that the geometric effect of Sn over Pd was very significant, by totally removing Pd-Pd pairs on which bridged CO was able to form[7]. In contrast, the effect on the heat of adsorption of linear CO, which is controlled by the electronic properties of the adsorption site (or ensemble), was modest.

Bimetallic Pt-Sn supported catalysts have been investigated in a large range of reactions such as selective hydrogenation of unsaturated compounds[8–13], dehydrogenation of light alkanes to alkenes where Sn is the most studied promoter of the platinum-based catalysts[14–18], low temperature oxidation of carbon monoxide[19–21]. A wide variety of parameters, mainly the Pt/Sn atomic ratio, the preparation procedure (e. g. conventional co-impregnation, chemical vapor deposition, polyalcohol reduction process), the nature of the precursors and of the support influence the electronic and geometric structure of the bimetallic particles and the formation of Pt_xSn_y alloys which determine the performances of the catalysts. For example, Taniya et al.[11] have prepared unsupported bimetallic PtSn-nanoparticles using a polyalcohol reduction process in order to avoid the influence of the metal-support interaction. Their catalytic behavior was examined for the selective hydrogenation of crotonaldehyde to crotyl alcohol (UOL). Pt_3Sn_1, Pt_1Sn_1 and Pt_1Sn_2 alloys were successively formed as the Pt/Sn atomic ratio increases. The UOL selectivity depends on the composition of the major Pt_xSn_y alloy species present in the catalyst. Highest total hydrogenation was obtained with Pt_3Sn_1 enhancing both C=C and C=O bonds hydrogenation. Pt_1Sn_1 alloy leads to the highest UOL selectivity which then decreases at the expense of butyraldehyde when Pt_1Sn_2 alloy is formed due to preferential C=C bond hydrogenation.

Kaylor et al. prepared Pt-Sn/SiO_2 and Pt-Sn/Al_2O_3 bimetallic supported catalysts with different Sn loading via incipient wetness impregnation or polyol method for propane dehydrogenation to propene[17]. Pt_3Sn and Pt_1Sn_1 alloys were detected by XRD whatever the preparation method and the support. Catalytic performances, particularly stability and selectivity to propene, depended on the strength of interaction of Sn with Pt relative to the support.

Pt-Sn alloy is also promising materials for Proton-Exchange Membrane Fuel Cells (PEM-FC), as Pt_3Sn_1 supported on carbon showed much improved resistance to CO poisoning as compared to Pt and many other alloys[22]. The improved resistance to CO poisoning was later attributed in part to lower CO adsorption coverage on the Pt sites[23]. As reported on our previous study[24], the heat of adsorption of CO on Pt in alumina-supported Pt-Sn alloy nanoparticles was measured to be 95 ± 5 kJ mol^{-1}, which is about half the value measured on plain Pt (180 ± 5 kJ mol^{-1}). This large difference makes the bonding of CO on the Pt of this Pt-Sn alloy similar to that measured on Cu°/alumina (85 ± 5 kJ mol^{-1})[25] and can explain the better resistance of Sn-modified Pt against CO poisoning. The sample above-mentioned was prepared from colloid-stabilized nanoparticles that exhibited the stoichiometry Pt_3Sn[26]. The exact stoichiometry of the derived alumina-supported Pt-Sn nanoparticles could not be determined accurately because a fraction of tin was converted to SnO_x species interacting with the alumina during the deposition/calcination process, while some of the Sn-containing ligand could have also decomposed and further reacted with the nanoparticles upon the final reduction[27]. This Pt_3Sn-like sample is therefore forthwith noted “Sn-poor” Pt-Sn/alumina. The colloidal procedure was used to prepare a Sn-rich sample (*vide infra*), except that the ratio of the Sn/Pt precursors was increased 12-fold as compared to the case of the Sn-poor material, aiming at a $PtSn_4$-like structure. Note that Pt_3Sn and $PtSn_4$ are the two extreme compositions of Pt-Sn intermetallic compounds, which also include Pt_1Sn_1, Pt_2Sn_3 and $PtSn_2$.

All the previous results emphasize the main role of the environment and electronic properties of surface Pt atoms modified by Sn. This was an incitement to focus in the present work on the use of CO adsorption monitored by *in situ* diffuse reflectance FT-IR spectroscopy (DRIFTS) as a means to characterize these properties. The IR experimental data are then compared to DFT models of CO adsorption applied to idealized surfaces and nanoparticles. The main aim is to highlight any possible difference between the Sn-rich and Sn-poor Pt-Sn nanoparticles in terms of electronic density probed by CO adsorption. To this end, IR

monitoring of CO adsorption is a powerful technique as it probes only the surface atoms, the most relevant for catalysis, and provides a statistical average over a large sample volume. However, CO adsorption can yet modify alloy surfaces, even at room temperature. Surface segregation was observed on Au-Pd nanoparticles as Pd, which forms a much stronger bond with CO than Au does, was gradually pulled towards the surface[28–30]. More, phase segregation induced by CO dissociation was also reported on Pt-Sn nanoparticles, as the resulting oxygen reacted with Sn forming tin oxide domains intimately mixed with Pt[31]. These phenomena are yet kinetically slow (timescale of tens of minutes) and can be mitigated by carrying out rapid analyses. The effect of CO dissociation can also be mitigated by carrying out CO adsorption in the presence of H_2, which probably removes any oxygen formed preventing Sn oxidation[31]. Such approach was fruitfully used in the present work. In addition, DFT calculations were performed to provide insights into the atomistic-level processes of CO adsorbate-induced segregation in Pt-Sn alloy surfaces with models representing Sn-poor and Sn-rich Pt-Sn nanoalloys.

II. Experimental and Theoretical methods

II.1. Experimental methods

Materials and gases

The preparations of the Pt/alumina and Sn-poor Pt-Sn/alumina materials have been reported elsewhere[26]. In brief, the method consisted in a two-step synthesis using a colloidal approach. A mixture of a Pt complex [$Pt(dba)_2$ (dba=dibenzylidene acetone)] and octylsilane, which plays the role of ligand, was used for the synthesis of Sn-free Pt monometallic nanoparticles. The Sn-poor Pt-Sn nanoparticles were obtained by contacting equimolar amounts of $Pt(dba)_2$ dried under vacuum and tributyltin hydride [$(n\text{-}Bu)_3SnH$] without the addition of any other ligand. The precursors were dissolved in dry tetrahydrofuran (THF) and pressurized with H_2 (3 bar) during 10 h at room temperature. A fraction of the Sn-precursors reduced forming Pt-Sn nanoparticles, while another fraction remained as ligands stabilizing the nanoparticles.

These colloidal suspensions were then used for the second step of the catalyst preparation. Following the evaporation of the solvent, a small volume of the suspension was

added to the γ-Al_2O_3 support (specific BET surface area 106 m^2/g) under continuous stirring and non-oxidative atmosphere and dried overnight under Ar. The dry crude catalysts were subsequently calcined under flowing dry air at 320 °C in order to remove most of the alkyl fragments. Note that a fraction of tin was converted to SnO_x species interacting with the alumina during this process[31]. An identical procedure was used for the preparation of the Sn-rich sample, except that the ratio of the Sn/Pt precursors was increased 12-fold as compared to the case of the Sn-poor material. The particle size distribution of this sample determined by TEM was narrow and centred around 1.8 nm (data not shown), that is essentially identical to those of the plain Pt and Sn-poor samples that were reported in our previous work[24].

High purity He and H_2 from Air Liquide (Alphagaz, 99.999% purity) further purified with using VICI® traps (models P-100-2 and P-200-2 for He and H_2, respectively) were used, which should have brought down O_2 level below 1 ppm. High purity CO (>99%, main impurity N_2 ~ 0.4 mol. % and H_2 ~ 0.5 mol. %) was used without further purification.

Diffuse Reflectance FT-IR spectroscopy analysis.

The DRIFTS experiments were performed at ambient pressure with a high temperature DRIFT cell (from Spectra-Tech®) fitted with KBr windows, using a collector assembly. A description and properties of the cell can be found elsewhere[32]. The spectrophotometer used was a Nicolet 6700 (ThermoFischer Scientific) fitted with a liquid-N_2 cooled MCT detector. The DRIFT spectra were recorded at a resolution of 4 cm^{-1} and 8 or 32 scans accumulation depending on the time-resolution desired.

The DRIFTS spectra are reported as log (1/R), where R is the sample reflectance. This pseudo-absorbance gives a better linear representation of the band intensity against surface coverage than that given by the Kubelka-Munk function for strongly absorbing media such as those based on metals supported on oxides[33]. The contribution of gas-phase CO was subtracted using a CO(g) spectrum collected at the reaction temperature over a SiC powder[34]. The temperature of the sample surface was determined according to a calibration curve obtained using an optical pyrometer as described elsewhere[32].

The sample was reduced *in situ* under a flow of 50 mL min^{-1} of pure H_2 at 400 °C for 30 min before going to the analysis temperature and introducing a flow of 2% CO/H_2. The production of methane was monitored using an IR gas-cell connected to the DRIFTS cell vent and was found to be negligible.

II.2. Theoretical details

Assessment of the energetics and electronic structures relevant for adsorbate-induced segregation phenomena are provided by periodic self-consistent DFT analysis using the Vienna ab initio simulation package (VASP)[35]. The exchange-correlation energy was calculated within the Perdew, Burke and Ernzerhof formulation of the generalized-gradient approximation (GGA-PBE)[36]. The valence electrons were treated explicitly, and their interactions with the ionic cores were described by the projector augmented-wave (PAW) method [37,38] , which allowed the use of a low energy cut off equal to 420 eV for the plane-wave basis. Super cell atomic positions were relaxed until the total energy differences decrease below 10^{-4} eV. In order to accurately capture weak interactions such as Van der Waals forces, DFT-D3 calculations including dispersion correction proposed by Grimme[39] were performed. The calculations of vibrational spectra of selected surface species were performed within harmonic approximation where only the CO center and its first and second neighbors (platinum and tin atoms) were considered in the Hessian matrix. This matrix was computed by the finite difference method followed by a diagonalization procedure. The eigenvalues of the resulting matrix led to the frequency values.

To calculate the segregation energies in presence and absence of CO gas, highly diluted systems formed by single Sn (Pt) atom in Pt (Sn) semi-infinite surfaces were considered. For Pt, three low index Pt surfaces (111), (100) and (110) were built from optimized FCC bulk structure. According to the work of Zhu *et al.*[40] these orientations are predicted to form the main facets of stable Pt nanoparticles under CO pressure. The bulk lattice constant was found to be of 3.96 Å which is in good agreement with experimental measured value of 3.92 Å[41]. Concerning Sn, experiments indicate that bulk Sn has both diamond (α-phase), and tetragonal (β-phase) structures[42]. Hörmann et al.[43] have reported that, independent of temperature, Sn nanoparticles smaller than 8 nm diameter always crystallize in the β-phase structure in

thermodynamic equilibrium. In addition, based on DFT calculations and thermodynamic considerations these authors have shown that the low-index (100) surfaces are the most stable. Based on these results, the low-index (100) surface was built from the optimized β-Sn (body-centered tetragonal, BCT) bulk structure. The calculated equilibrium lattice constants (a, b = 5.94 Å, c = 3.21 Å) were found to be slightly overestimated compared to the experimental values (a = b = 5.83 Å, c = 3.18 Å at 298.15 K)[44], but in good agreement with reported theoretical results[27,31,34]. The surface slabs consist of 3 x 3 unit cells separated by 15 Å of vacuum space for Pt surfaces and 2 x 3 unit cells with 15 Å of vacuum space for Sn surface. The Brillouin zone integrations were performed on a Monkhorst–Pack (3 x 3 x 1) and (2 x 3 x 1) k-point mesh for Pt and Sn surfaces, respectively. Total relaxation of all metallic atoms in the top four layers of the slab and the adsorbed CO molecule was allowed. The bottom two layers were constrained at the bulk geometries. Once the surfaces were optimized, Sn and Pt single impurities were substituted in different layers of the host Pt and Sn surfaces, respectively, and total energies were calculated. The segregation energy (E_{seg}) of Sn (Pt) in Pt (Sn) matrix was defined by equation 1.

$$E_{seg.} = [E_{Pt\text{-}Sn(x\text{-}layer)} - E_{Pt\text{-}Sn\ (4th\text{-}layer)}] \quad (Eq.1)$$

where $E_{Pt\text{-}Sn\ (x\text{-}layer)}$ represents the total energy of the Pt-Sn alloy system with Sn(Pt) atoms located in the upper x Pt(Sn) layers (x= 1, 2 or 3), and $E_{Pt\text{-}Sn\ (4th\text{-}layer)}$ represents the total energy of the Pt-Sn alloy system with the Sn(Pt) atom located in the 4th Pt(Sn) layer, which corresponds to the center of the slab, i.e. to the bulk-like position. In the presence of adsorbed CO molecule, the segregation energies were calculated by considering the energetically most stable configuration.

To study the CO probe adsorption mechanisms and its vibrational frequencies on Pt-Sn nanoalloyed system, pure Pt and Pt-Sn clusters of different Sn ratio were modeled. Cubic cell with the side of 2 nm was chosen to provide enough spacing between metal clusters in the neighboring repeated cells. Truncated-cubo-octahedral (TOH) shape of 38 atoms was cut from bulk *fcc* metal presenting (111) and (100) facets. According to our previous theoretical studies[47,48], this selected size and structure offers a good compromise between time calculation and theoretical level of accuracy. To model Sn-rich ($PtSn_4$) and Sn-poor (Pt_3Sn) Pt-Sn nanoparticles, TOH_Pt_7Sn_{31} and TOH_$Pt_{29}Sn_9$ clusters were considered, respectively. As will be argued bellow, the choice of the selected configurations was based on the study of the energetics of the segregation and mixing of Pt-Sn system. Brillouin zone integrations were

performed at the Gamma point and all atoms were relaxed during geometry optimizations. According to their coordination numbers, the surface atoms may have two coordination numbers: 6 for edge position and 9 for center face position. Hereafter, we define all possible CO adsorption sites as follows: two top sites, over surface atom located at an edge position (top-ed) or at a center face position (top-fc); two bridge sites, between two atoms located at the edge position (BDG-ed-ed) and between edge and facet atoms (BDG-ed-fc); three-fold sites between three adjacent atoms on the (111) facet and four-fold sites between four adjacent atoms on the (100) facet. The adsorption energy of CO molecule was calculated by equation 2:

$$E_{ads}=E_{cluster+CO} - E_{CO} - E_{cluster} \qquad (Eq.2)$$

where $E_{cluster+CO}$ is the total energy of the CO adsorbed on the metallic cluster, E_{CO} and $E_{cluster}$ are the total energies of free CO and metal cluster, respectively.

III. Results and discussions

III.1. Experimental results

DRIFTS spectra obtained between 200 °C down to 50 °C over the Sn-rich Pt-Sn/alumina under a flow of 2% CO/H_2 are shown in Figure 1. H_2 was kept in the feed to limit the phase segregation of the Pt-Sn nanoparticles due to minute CO dissociation and O reaction with Sn[27,49]. The spectra recorded at 200 °C exhibited a main band at 2032 cm^{-1}, which shifted towards 2040 cm^{-1} at 100 °C. This band is assigned to linear CO adsorbed on Pt in a Pt-Sn phase[27,50].

From 200 °C down to 100 °C the band remained mostly symmetric, indicating a homogeneity in the nature of the Pt sites present. However, the band developed a shoulder on the high wavenumber side below 100°C that was clearly visible at 50 °C. (Red spectrum in Fig. 1). This shoulder and change of the band shape are especially visible when comparing the spectra at 150 °C and 50 °C (Inset in Fig. 1). This observation is indicative of the presence of plain Pt nanoparticles, likely developing around SnO_x domains, following the dissociation of CO leading to the oxidation of tin and carbon deposition, as was already reported for the Sn-poor Pt-Sn/alumina sample[27]. The spectra below 100 °C are thus associated with a mixture of Pt/SnO_x and Pt-Sn phases and do not represent only the intermetallic compound. In fact,

bridging CO becomes visible at 1885 cm^{-1} for the spectrum collected at 50 °C, confirming the formation of Pt-Pt pairs and the aggregation of Pt atoms at this temperature[51–53].

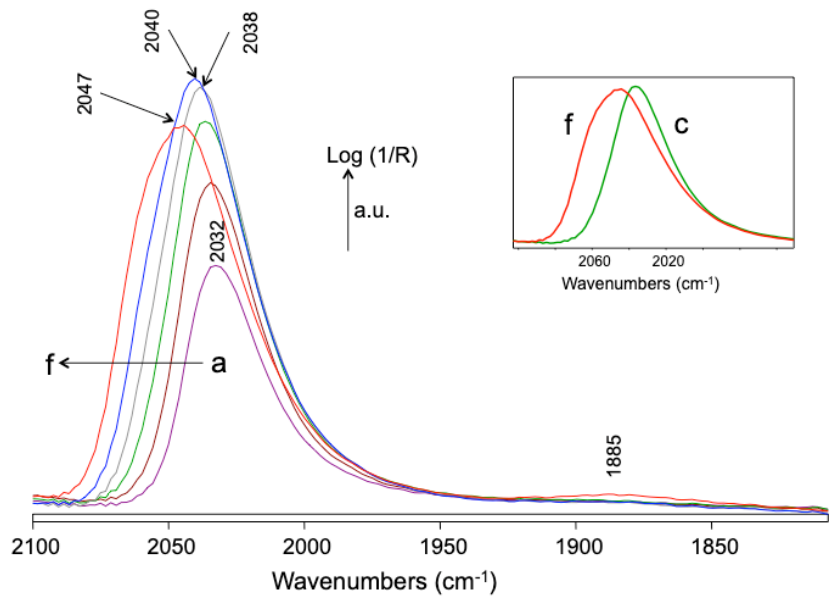

Figure 1. DRIFTS in situ spectra during CO adsorption over Sn-rich Pt-Sn/alumina at various temperatures: (a) 200 °C, (b) 175 °C, (c) 150 °C, (d) 125 °C, (e) 100 °C and (f) 50 °C. The inset is a zoom in on the spectra at (c) 150°C and (f) 50°C. Feed: 2 % CO in H_2. The spectrum of the sample reduced under H_2 at 400 °C was used as background

The generalized Temkin model used to determine the heats of adsorption at zero and full CO coverage has been described in details elsewhere[7,54]. The model assumes that the heat of adsorption linearly increases with decreasing coverage. The method consists in optimizing the values of adsorption heats at zero and full coverage to obtain the best agreement between the experimental and model curves representing the surface coverage as a function of temperature (Figure 2). According to Figures 1 and 2 the full coverage by CO was assumed to be achieved at 100 °C, in view of the evolution of the band areas (Figure 1 and 2). The adsorption heats at zero and full coverage thus determined for the Sn-rich Pt-Sn/alumina were 85 ± 5 and 75 ± 5 kJ mol^{-1}, respectively. These values are reported in Table 1 and compared to those measured earlier on alumina-supported Pt and Sn-poor Pt-Sn.

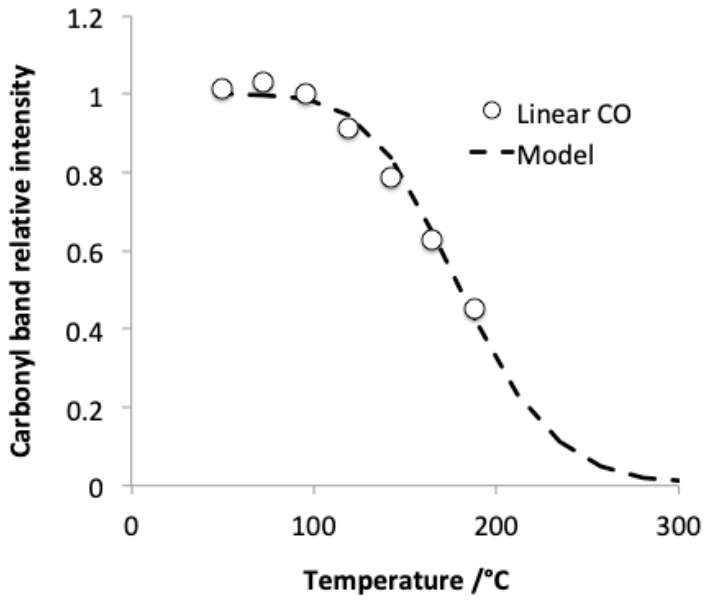

Figure 2. CO relative coverage as a function of temperature on the Sn-rich Pt-Sn/alumina (o) and corresponding Temkin model (dotted line). Full coverage was assumed to be achieved at 100 °C. The spectra at 75 and 50 °C also contained a non-negligible fraction of plain Pt domains alongside Pt-Sn.

Table 1. Adsorption heats for linear CO on Pt in various samples and the corresponding wavenumber of CO at full coverage.

	Adsorption heat at zero coverage	Adsorption heat at full coverage	CO stretch at full coverage
	± 5 kJ/mol	± 5 kJ/mol	± 2 cm^{-1}
Pt [a]	180	85	2075
Sn-poor Pt-Sn [a]	95	75	2054
Sn-rich Pt-Sn	85	75	2039

[a] see reference [24]

No alloy segregation into Pt + SnO_x can be observed above 100 °C in the presence of both CO and H_2. However, a rather slow but gradual signal increase at essentially constant wavenumber was observed following the introduction of CO in the H_2 feed on the pre-reduced Sn-rich Pt-Sn sample at higher temperatures. A set of spectra collected at 420 °C is presented in Figure 3 to exemplify this observation. This high temperature was chosen because it allowed observing the phenomenon over a reasonably short period of time of about 8 minutes. The

observed signal increase was not due to the time required to flush the gas cell dead volume from pure H_2 to the 2 % CO/H_2 mixture, which requires less than 15 s.

Over the 8-min period the band hardly shifted from 2029 to 2032 cm^{-1}, which is within the experimental error. However, the band intensity grew by about 50 %, indicating a large increase of the concentration of Pt atoms at the surface of the Sn-rich Pt-Sn/alumina. This observation indicates that Pt was pulled to the surface from the bulk due to the formation of Pt-CO bond. A similar surface segregation phenomenon has been reported for Pd-Au alloys upon CO gas exposure[28–30]. After 8 min the signal was stable, indicating that a new equilibrium between surface and bulk Pt atoms had been reached. It is important to note that this surface segregation (implying variations of the Pt and Sn surface and bulk concentrations of the Pt-Sn nanoparticles) is different from the alloy segregation due to CO dissociation observed in Figure 1 (implying the formation of separate Pt and SnO_x domains).

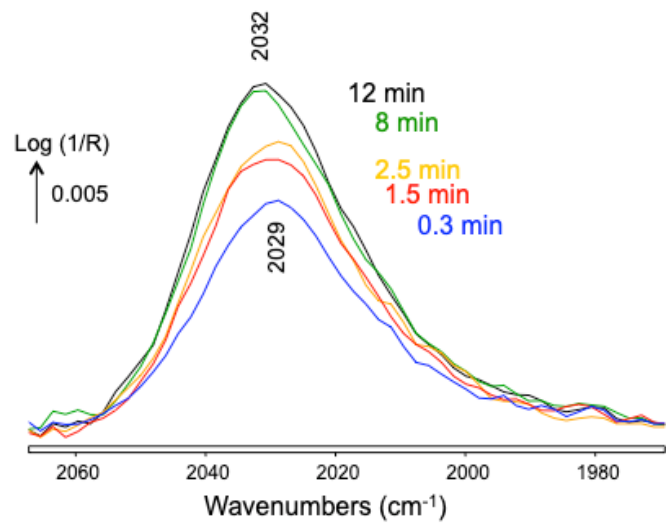

Figure 3. Evolution of the Pt-CO DRIFTS signal on the Sn-rich Pt-Sn/alumina at 420 °C with time following the introduction of CO in the H_2 feed at 0 min. Feed: 2 % CO in H_2. The spectrum of the sample reduced under H_2 at 420 °C was used as background

III.2. Theoretical results

Segregation phenomenon

In order to get an insight into the CO induced segregation of Sn and Pt in Pt-Sn, we performed DFT calculations of the segregation energies of Sn atom on Pt (111), (100) and (110) surfaces and of Pt atom on Sn(100) surface (calculated from Eq. (1)). The analyzed systems could represent both highly diluted Sn-poor and Sn-rich Pt-Sn systems, respectively. Figure 4 a. reports the evolutions of the segregation energies of one Sn atom as a function of its position in the three platinum surfaces and Figure 4b reports the results for Pt in Sn (100) surface. These evolutions of segregation energies (E_{seg}) are calculated both in the presence and in the absence (vacuum conditions) of CO gas.

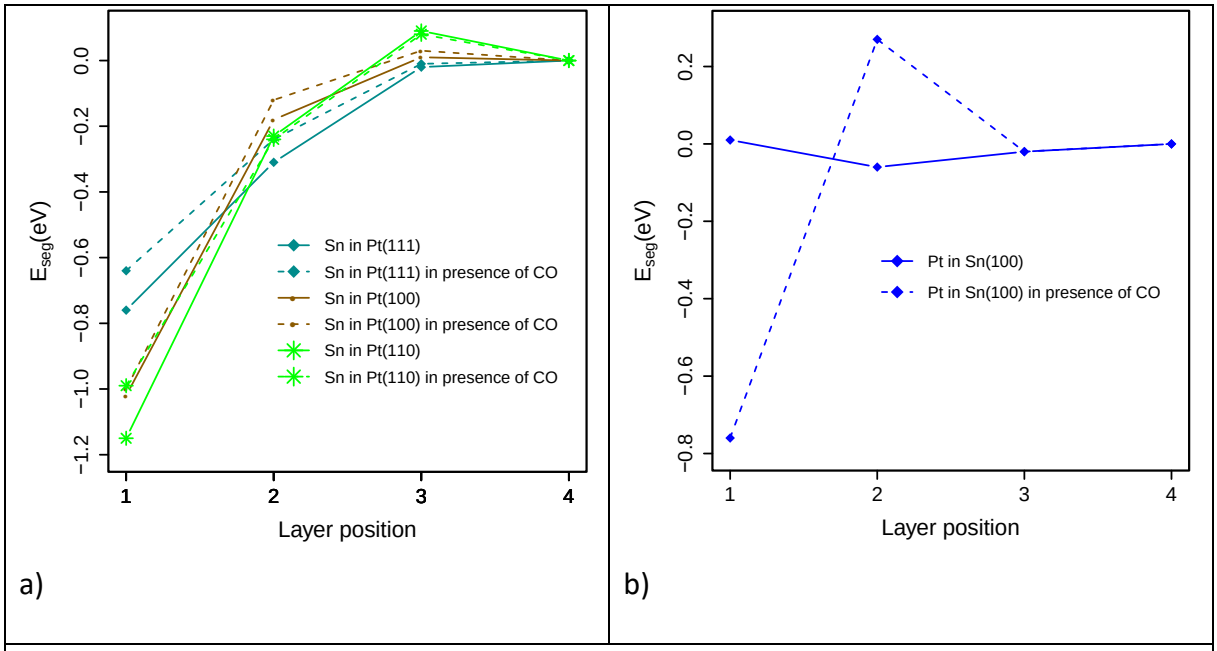

Figure 4: Segregation energies in absence (full lines) and presence (dashed lines) of CO a): Sn in Pt(111), (100) and (110). b) Pt in Sn(100).

Under vacuum conditions, the single Sn presents a similar behavior on the three facets; it is highly stable in the first layer of the three considered surfaces (E_{seg} = -0.8 eV/atom, -1.01 eV/atom and -1.18 eV/atom for (111), (100) and (110) surface, respectively). Interestingly, the more open the surface is, the more stable the Sn in the first layer of Pt. This stability gets worse when Sn is located on the sub-surface layer (second layer position of the slab) and in

the Pt bulk (third and fourth layers). These results can be explained by two facts. On one hand, the lower surface energy of Sn compared to that of Pt favors the segregation of Sn toward the upper surface layer; experimental values are 0.709 J m^{-2} for Sn and 2.489 J m^{-2} for Pt[55]. On the other hand, because of the higher atomic radius of Sn compared to Pt (1.55 Å vs. 1.39 Å)[41], the isolated Sn atoms prefer occupying under-coordinated surface sites. The segregation energy of Sn was also calculated in presence of CO adsorbed on the surfaces of Pt. As expected, CO does not directly interact with Sn atom and mostly prefers the top site of Pt atoms. As shown by the dashed lines in Figure 4a. the presence of CO slightly disturbs the stability of the system but do not change the chemical atomic ordering on the surface.

Considering Pt in Sn(100) surface, the Figure 4b shows the evolution of segregation energy in presence and in absence of CO. Under vacuum, the system shows better stability of Pt in the second layer then in the surface and the bulk. In the subsurface layer (2nd layer) of Sn surface, the system is predicted to be slightly more stable (-0.06 eV). The energetically favorable location of the Pt atom at the second layer of Sn matrix can be explained by the fact that the Pt has higher surface energy and higher cohesive energy than Sn and that its presence in the second layer allows releasing the elastic energy due to the atomic size mismatch. Interestingly, under gas, the segregation behavior drastically changes. Indeed, in the presence of one CO adsorbed on top of isolated Pt, this latter becomes highly stable on the surface while subsurface Pt become highly instable (E_{seg}= -0.76 eV/atom and +0.27 eV/atom when located on the first and second layers Sn surface, respectively). So, one can expect that for Pt-Sn nanoparticles exposed to CO gas, Pt atoms are either on the surface directly interacting with CO or in the bulk. This result corroborates well with the evolution of our experimental Pt-CO DRIFTS signal on the Sn-rich Pt-Sn/alumina (Figure 3) indicating that Pt was pulled to the surface from the bulk due to the formation of Pt-CO bond.

To go further and to learn more about the mixing tendency of Pt in Sn surface, we compared the stability of one Pt dimer and two isolated Pt atoms in the presence and in the absence of interacting CO. The calculated total energies predict that for diluted systems (Sn-rich Pt-Sn) the formation of isolated Pt surrounded by Sn atoms is more favorable than the formation of pure Pt ensembles.

Electronic structure analysis

In order to examine the local effect of CO-induced segregation of Pt atom on the topmost surface layer of Sn-rich and Sn-poor Pt-Sn alloys, the local density of states (DOS) were calculated, in presence and in absence of adsorbed CO. For the following analyses, the pure Pt(100) and Sn(100) surfaces as well as the Sn(100) with one diluted Pt on the surface (representing Sn-rich Pt-Sn alloy) are selected. Figure 5 shows the *d*-band DOS for diluted Pt atom and the *s,p*-bands of first neighboring Sn atom in the upper layer of the Sn(100) surface. These DOSs are calculated under vacuum and are compared to DOSs calculated for pure Sn(100) and Pt(100) metal surfaces.

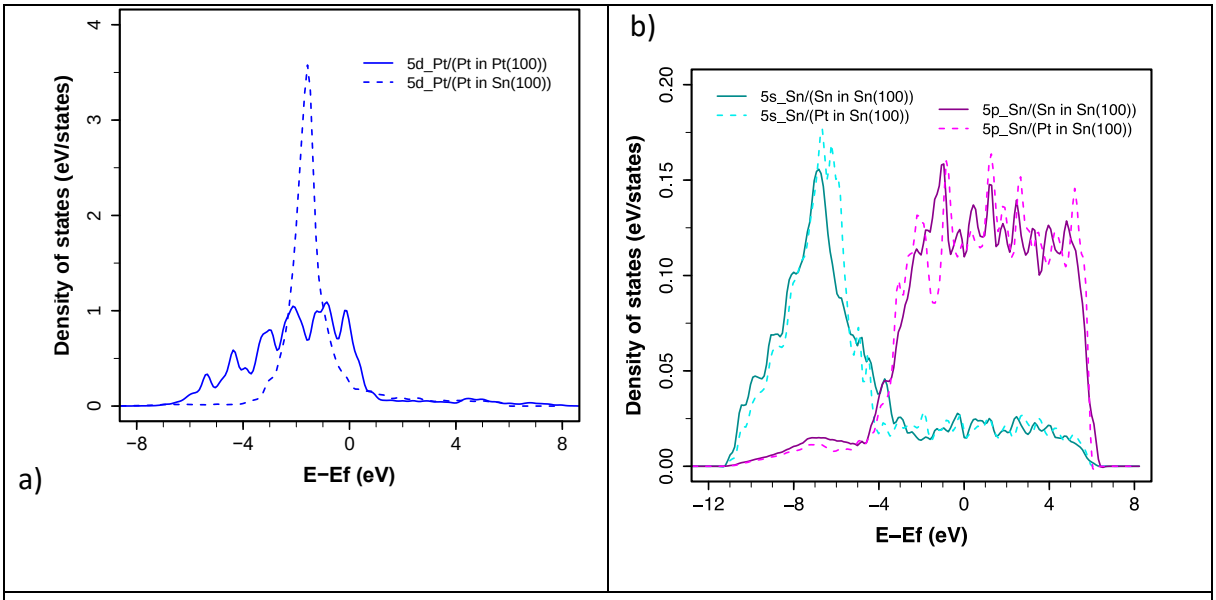

Figure 5: Density of states (DOS) calculated under vacuum. (a) 5d-band of Pt atom located in the first layer of Pt(100) surface (full line) and diluted in the topmost layer of the Sn(100) surface (dashed line). (b) 5s (cyan lines) and 5p (purple lines) band DOSs for Sn atom located in the topmost layer of pure Sn(100) surface (full lines) and in the first neighboring site of diluted Pt (dashed lines) in Sn(100) surface.

Compared to pure Pt surface which has a large density of unoccupied d states above the Fermi level (Figure 5a), the isolated Pt surrounded by Sn atoms (Sn-rich alloy) has no more unoccupied energy states and its d-band DOS becomes very narrow. For the surrounding Sn atom (see Figure 5b), the *s* and *p* bands are very slightly disturbed but a small increase of the

intensity of occupied states of *s*-band can be distinguishable for the energy range between -8 and -5 eV.

As expected, in presence of CO on the top of the Pt atom surrounded by Sn, significant changes are recorded. In Figure 6 are reported the changes in DOSs of Pt and interacting CO molecule. Fig.6a shows a strong shift of the d-band center of Pt away from the Fermi level induced by the presence of CO. In addition, a significant hybridization is evidenced between *p*-band of CO and *d*-band of Pt in the conduction band -7.5 eV and -8.5 eV and valance band 2.5 eV regions. This corresponds to the bonding and antibonding states between *p* orbital of CO and *d* orbital of Pt. The additional peak appearing at the higher edge of the d-band DOS of the platinum surface atom (around 2.5 eV) (Figure 6a) could be the signature of a covalent CO–Pt bond where charge transfer may occur. To analyze the effect of Sn ensemble on the electronic structure of adsorbed CO, the Figure 6b. reports the superposition of the 2*p*-band orbitals of CO adsorbed on Pt atom surrounded by 1 Sn atom (Sn-poor Pt-Sn) and by 7 Sn atoms (Sn-rich Pt-Sn). The increase of Sn environment induces a significant shift toward the Fermi level of the peak located around 3.5 eV (see insert). The shift of this peak, corresponding to the $2\Pi^*$ orbital of CO, indicates that Sn ensemble decreases the Pt-CO bonding which is in line with the measured heat of adsorption found to decrease when Sn content increase. Thus, the introduction of Sn improves the resistance against CO-poisoning of Pt surfaces.

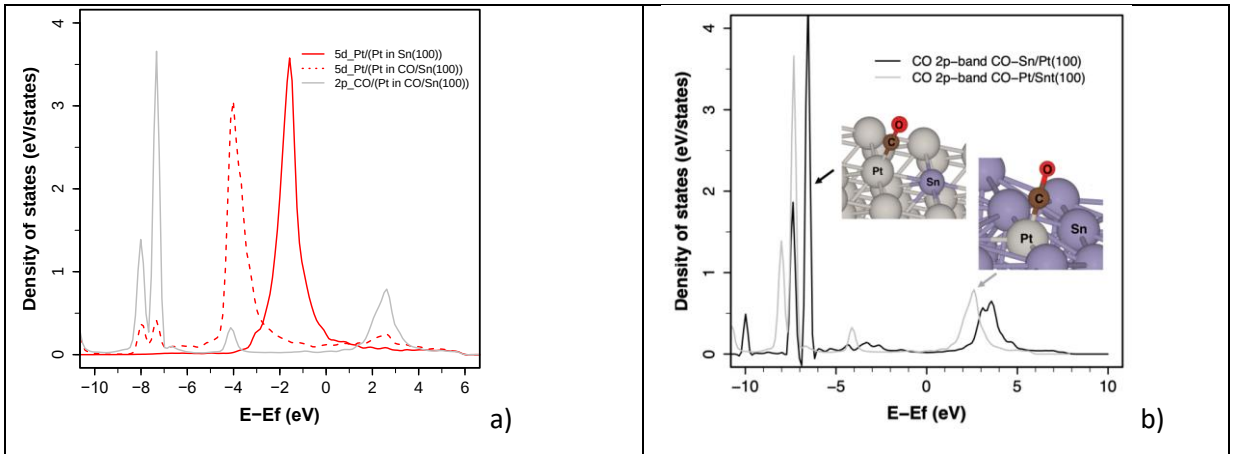

Fig. 6. Density of states (DOS) of a) Pt in Sn(100) surface (representing the Sn-rich Pt-Sn alloy) in red lines before (full line) and after (dashed line) CO adsorption. The dashed gray line represents the 2p-orbitals of adsorbed CO molecule.

b) Comparison of 2p orbitals of carbon atom of CO molecule adsorbed on Pt in Sn-poor surface alloy (black line) and in Sn-rich Pt-Sn surface alloy (gray line).

In order to examine the charge transfer between CO and Pt, the charge density differences before and after the carbon monoxide adsorption were calculated by equation 3:

$$\Delta\rho = \rho_{(slab+CO)} - \rho_{(slab)} - \rho_{(CO)} \qquad \text{Eq.3}$$

where $\rho_{(slab+CO)}$ represents the charge density of the CO adsorbed surface, $\rho_{(slab)}$ and $\rho_{(CO)}$ are the charge density of the clean surface and of the absorbate CO molecular with geometries fixed from the optimized CO-adsorbed surface, respectively.

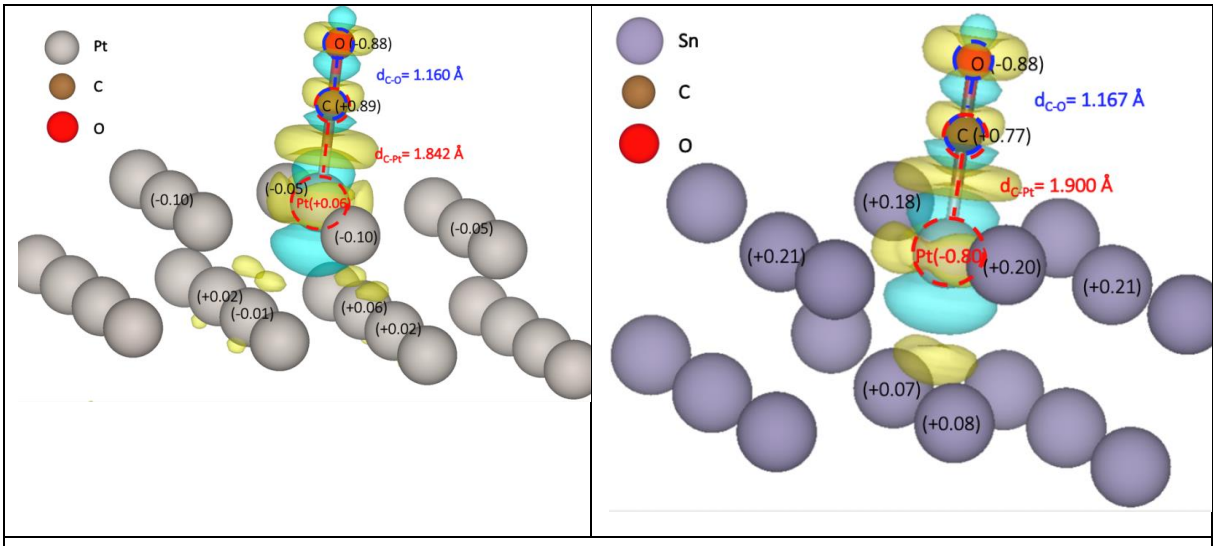

Figure 7. : Charge density difference plots for carbon monoxide adsorption on top site of Pt atom in (left) Pt(100) pure metal surface, (right) PtSn(100) alloy surface. The numerical values indicate calculated Bader charges. Blue (yellow) areas represent the electron accumulation (depletion) regions. d_{c-o} is the distance between carbon and oxygen atom; d_{c-Pt} is the distance between the carbon atom and the bonded Pt atom. Pt and Sn atoms are displayed as grey and indigo spheres, respectively.

In Figure 7 are represented the charge density difference for CO adsorbed on pure Pt(100) and on a diluted Pt on Sn(100) surface. In the later surface $\Delta\rho$ was found to be mostly located on the Pt atom and its interacting CO; the neighboring Sn atoms not seem to be affected by the presence of CO. This corroborates well with the small perturbation found on the DOSs of *s* and *p* orbitals reported in Figure 5b. However, compared to Pt(100) surface, the $\Delta\rho$ of PtSn(100) shows important electron transfer mainly from surface Sn atoms to single Pt (more than 0.8

é) which induces a strong electron accumulation around Pt. This charge transfer is expected as the electronegativity of Pt is much higher than that of Sn (2.28 for Pt *vs.* 1.96 for Sn). The charge transfer from Pt to CO is found to be small; about 0.12 é with more important charge depletion in the Pt-CO bond. This depletion is accompanied by a significant prolongation of Pt-C bond distance (from 1.842 Å in CO-Pt(100) to 1.900 Å in CO-PtSn(100) surface) which has also an incidence on the C-O bond length (elongation of 0.007 Å). The weakening of C-O bond is in line with the experimental prediction of CO dissociation over Pt-Sn nanoalloys inducing the formation of SnO_x domains.

CO on Pt-Sn nano-clusters: Adsorption and vibrational frequencies

The above energetic and electronic studies of Pt and Sn in Pt-Sn alloys using semi-infinite surface models evidenced characteristics that could be extrapolated to nanosized system:

i) The interaction of CO with Sn-Pt induces the surface segregation of Pt from the bulk.

ii) In the presence as in the absence of CO, Sn prefers to occupy low coordinated sites of the top most surface layer of Sn-poor Pt-Sn nanoalloys.

Based on these results, truncated cuboctahedral nano-clusters of Pt-Sn were modeled to monitor the CO interactions on Pt-Sn nanoalloys as a function of surrounding chemical environment and to extract information of the structural arrangement under reacting gas. Pure Pt (TOH_Pt_{38}), Sn-rich (TOH_Pt_7Sn_{31}) and Sn-poor (TOH_$Pt_{29}Sn_9$) Pt-Sn clusters were considered to study the adsorption mechanisms of probe CO molecule and to calculate the variation of adsorption energies and vibrational frequencies as a function of surface composition. TOH_Pt_7Sn_{31} is a core-shell-like structure where 6 Pt atoms are located in the bulk and 1 Pt surface atom interacts with CO. All 31 Sn atoms are located in the surface. For TOH_$Pt_{29}Sn_9$ 9 Sn atoms occupy the edge sites of the TOH surface structure and all the rest of atoms are Pt. In Figure 8 are illustrated the geometry optimized configurations of CO for which energetic and vibrational parameters are gathered in Table 2. As CO does not adsorb on Sn sites, the unique selected configuration for Sn-rich Pt-Sn (TOH_Pt_7Sn_{31}) corresponds to CO adsorbed on top site of Pt atom. Over pure Pt (TOH_Pt_{38}) and Sn-poor Pt-Sn (TOH_$Pt_{29}Sn_9$),

three Pt adsorbed sites of CO are found to be favorable: top_ed, top-fc and BDG-ed-fc sites. The 3-fold and 4-fold sites were found to be unfavorable for the adsorption of CO.

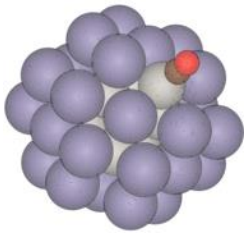	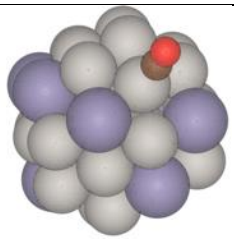	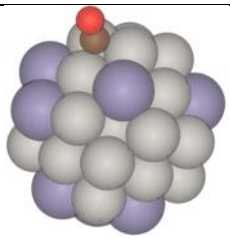	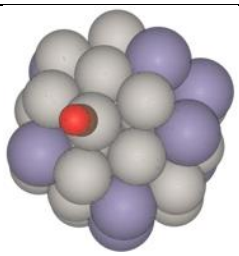
TOH_Pt_7Sn_{31} (CO-Pt(top _ed))	**TOH_$Pt_{29}Sn_9$ (CO-Pt(top-fc))**	**TOH_$Pt_{29}Sn_9$ (CO-Pt(BDG-ed-fc)**	**TOH_$Pt_{29}Sn_9$ (CO-Pt(top _ed))**
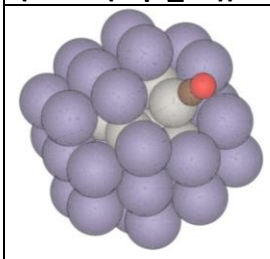	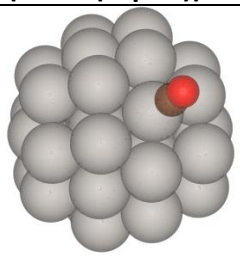	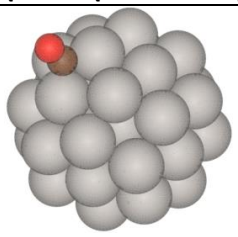	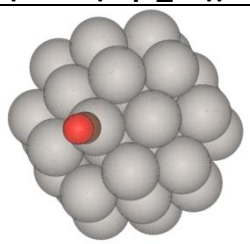
TOH_Pt_7Sn_{31} (CO-Pt(top _fc))	**TOH_Pt_{38} (CO-Pt(top-fc))**	**TOH_Pt_{38} (CO-Pt(BDG-ed-fc)**	**TOH_Pt_{38} (CO-Pt(top _ed))**

Figure 8: Illustration of the different CO adsorption sites on various Pt-Sn cluster configurations. Pt, Sn, C and O atoms are displayed as grey, indigo, brown and red spheres, respectively.

Table 2: DFT-D3 calculated adsorption energies and frequencies of CO adsorbed on PtSn nanoclusters. A scaling factor of 1.025 was applied to the calculated frequency values which corresponds to the adjustment of the calculated frequency of CO on pure Pt nanocluster with the observed experimental value.

Clusters	**CO adsorption site**	**Eads (eV)**	**DFT calculated ν_{CO} (cm^{-1})**	**Experimental ν_{CO} (cm-1)**
TOH_Pt_{38}	Top Pt (edge site)	-2.20	**2075**	**2075**
	Top Pt (Fc site)	-2.02	2096	----
	Bridge Pt	-2.10	1895	1885

TOH_$Pt_{29}Sn_9$	Top Pt (edge site)	-2.18	2049	2054
	Top Pt (Fc site)	-1.72	2075	---
	Bridge Pt	-1.60	1871	-----
TOH_Pt7Sn31	Top Pt (edge site)	-1.53	2035	2039
	Top Pt (Fc site)	-0.86	2038	

DFT optimizations show that on pure Pt nanocluster the CO prefers to adsorb on the top site rather than on the bridge site. The top of Pt atom located at the edge position is found to be the most favorable site with adsorption energy value of -2.20 eV. The adsorption energy on top of Pt located at the center face is predicted to be lower by 0.18 eV. For Pt-Sn, the preference of CO to the top site of under-coordinated Pt atoms remains true but alloying Pt with Sn induces a decrease in the adsorption energies. On TOH_$Pt_{29}Sn_9$ the adsorption energy of CO is found to decrease by about 0.02 eV on top Pt site by 0.5 eV on bridge one in comparison to pure Pt nanoclusters. The energy decrease is found to be more drastic on Sn-rich Pt-Sn nanocluster where the adsorption energy of linear CO (see Figure 8, TOH_Pt_7Sn_{31} (CO-Pt(top _ed) and TOH_Pt_7Sn_{31} (CO-Pt(top _fc)) is calculated to be of -1.53 eV and -0.86 eV on Pt segregating on edge and top position, respectively. The decay in adsorption energy is from 0.73 eV to 1.34 eV lower than the adsorption energy on pure Pt nanoclusters which is in line with the experimental measurements of heat of adsorptions.

To go further in the comparison between calculated and experimental features of CO adsorbed on Pt-Sn system, vibrational frequencies were calculated and reported in Table 2. The calculated harmonic frequencies at the GGA/PBE level of adsorbed CO are below those observed in the DRIFTS experiments. At least, this is partially due to the considered low CO coverage case where dipole-dipole interaction is minimized (red-shift spectra) and for which the molecules are more strongly bonded to the surface (increased back-donation resulting in a red shift of the stretching frequency). To facilitate the comparison, a scaling factor of 1.025 was applied which corresponds to the adjustment of the calculated frequency of CO on pure Pt nanocluster (TOH_Pt_{38} (CO-Pt(top _ed)) to the value of ν_{CO} of 2075 cm^{-1}, experimentally measured for CO linearly adsorbed on pure Pt nanoparticles (see Table 1). Interestingly, for TOH_$Pt_{29}Sn_9$ and TOH_Pt_7Sn_{31} nanoclusters, the results of frequency calculations of CO

adsorbed on top Pt edge atom show the same red shift as observed experimentally. The values of 2049 cm^{-1} and 2035 cm^{-1}, depicted in Table 2, correspond very well with the experimental observed IR bands of ν_{CO} in Sn-poor Pt-Sn (2054 cm^{-1}) and Sn-rich Pt-Sn alloys (2039 cm^{-1}), respectively. These results show that from DFT calculations we can reasonably assigned the various bands observed in DRIFTS spectra of Pt-Sn nanoparticles and describe their evolution induced by surface segregation phenomena. The concordance between experimental data and experimental results provides a clear picture of the surface chemical ordering of Pt-Sn nanoalloys and their evolution under reactive CO gas.

IV. Conclusion

CO adsorption on Sn-rich Pt-Sn nanoparticles supported on alumina allowed observing two modes of segregation depending on the experimental conditions. The first mode, observed at temperatures above 100 °C upon the introduction of CO in the H_2 feed, is a surface segregation related to an enrichment of the surface of the Pt-Sn nanoparticles with Pt. This phenomenon, which does not lead to any significant band shift or shape change, is triggered by the formation of Pt-CO bond increasing the stability of Pt at the surface of the Pt-Sn nanoparticles. This Pt surface segregation was confirmed by DFT calculations on modeled Sn-rich and Sn-poor Pt-Sn alloy surfaces where geometric and electronic structure analyses highlighted the observed affinity of Pt to the CO gas. The second segregation phenomenon was observed experimentally at temperatures lower than 100 °C in CO + H_2 feed and led to a significant change of band shape and shift was due to the formation of Pt and SnOx domains triggered by CO dissociation. To learn more about the first segregation phenomenon, the heats of CO adsorption was determined by DRIFTS over various Pt-Sn surface. The DRIFTS data showed a gradual decay of the linear wavenumber from plain Pt (2075 cm^{-1}), through a Sn-poor Pt-Sn (2054 cm^{-1}) and to a Sn-rich Pt-Sn (2039 cm^{-1}). The heat of adsorption at zero coverage also decayed in a parallel manner, from plain Pt (185 kJ mol^{-1}), through Sn-poor Pt-Sn (95 kJ mol^{-1}) and to Sn-rich Pt-Sn (85 kJ mol^{-1}). DFT calculated adsorption energies as well as frequency calculations are fully consistent with the experimental results and thus provide an accurate model at the atomic level of Pt-Sn surface nanoparticles. Moreover, electronic structure analyses show significant charge transfer from Sn to Pt accompanied by a shift away (toward) the Fermi level of the bonding (antibonding) orbitals of the adsorbed CO. This result indicates that Sn decreases the Pt-CO bonding which is in line with the measured heat of adsorption

found to decrease when increasing Sn composition, thereby improving the CO-poisoning resistance of Pt surface atoms.

Acknowledgements:

A. Moscu and C. Theodoridi are acknowledged for sample preparation and help in carrying out the IR experiments, respectively. L. Veyre is acknowledged for the TEM analysis. This work was granted access to the HPC resources of [CCRT/CINES/IDRIS] under the allocation 2019 [x2019087369] made by GENCI (Grand Equipement National de Calcul Intensif).

References

[1] S. Zafeiratos, S. Piccinin, D. Teschner, Alloys in catalysis: phase separation and surface segregation phenomena in response to the reactive environment. *Catal. Sci. Technol.* **2012**, *2*, 1787–1801.

[2] A. Dasgupta, R. M. Rioux, Intermetallics in catalysis: An exciting subset of multimetallic catalysts. *Catal. Today* **2019**, *330*, 2–15.

[3] M. F. M. F. Juárez, G. Soldano, H. Guesmi, F. Tielens, E. Santos, Catalytic properties of Au electrodes modified by an underlayer of Pd. *Surf. Sci.* **2015**, *631*, 235–247.

[4] S. Verdier, B. Didillon, S. Morin, D. Uzio, Pd-Sn/Al2O3 catalysts from colloidal oxide synthesis - II. Surface characterization and catalytic properties for buta-1,3-diene selective hydrogenation. *J. Catal.* **2003**, *218*, 288–295.

[5] H. R. Aduriz, P. Bodnariuk, B. Coq, F. Figueras, Alumina-supported bimetallics Bof palladium alloyed with germanium, tin, lead or antimony, from organometallic precursors .2. Gas-phase hydrogenation of 2-methyl-1-buten-3-yne (valylene) and 2-methyl-1,3-butadiene (isoprene). *J. Catal.* **1991**, *129*, 47–57.

[6] S. H. Choi, J. S. Lee, XAFS study of tin modification of supported palladium catalyst for 1,3-butadiene hydrogenation in the presence of 1-butene. *J. Catal.* **2000**, *193*, 176–185.

[7] I. Jbir, J. Couble, S. Khaddar-Zine, Z. Ksibi, F. Meunier, D. Bianchi, Individual Heat of Adsorption of Adsorbed CO Species on Palladium and Pd-Sn Nanoparticles Supported on Al2O3 by Using Temperature-Programmed Adsorption Equilibrium Methods. *ACS Catal.* **2016**, *6*, 2545–2558.

[8] P. Mäki-Arvela, J. Hájek, T. Salmi, D. Y. Murzin, Chemoselective hydrogenation of carbonyl compounds over heterogeneous catalysts. *Appl. Catal. A Gen.* **2005**, *292*, 1–49.

[9] G. F. Santori, M. L. Casella, G. J. Siri, H. R. Adúriz, O. A. Ferretti, Hydrogenation of

crotonaldehyde on Pt/SiO2 catalysts modified with tin added via surface organometallic chemistry on metals techniques. *Appl. Catal. A Gen.* **2000**, *197*, 141–149.

[10] J. L. Margitfalvi, G. Vankó, I. Borbáth, A. Tompos, A. Vértes, Characterization of Sn-Pt/SiO2 catalysts used in selective hydrogenation of crotonaldehyde by Mossbauer spectroscopy. *J. Catal.* **2000**, *190*, 474–477.

[11] K. Taniya, H. Jinno, M. Kishida, Y. Ichihashi, S. Nishiyama, Preparation of Sn-modified silica-coated Pt catalysts: A new Pt-Sn bimetallic model catalyst for selective hydrogenation of crotonaldehyde. *J. Catal.* **2012**, *288*, 84–91.

[12] J. Llorca, P. Ramirez de la Piscina, J. Sales, N. Homs, Activation of carbon dioxide by a silica-supported platinum-tin bimetallic complex. *Chem. Commun.* **1994**, *22*, 2555–2556.

[13] J. Ruiz-Martínez, F. Coloma, A. Sepúlveda-Escribano, J. A. Anderson, F. Rodríguez-Reinoso, Effect of tin content and reduction temperature on the catalytic behaviour of PtSn/TiO2 catalysts in the vapour-phase hydrogenation of crotonaldehyde. *Catal. Today* **2008**, *133–135*, 35–41.

[14] J. J. H. B. Sattler, J. Ruiz-Martinez, E. Santillan-Jimenez, B. M. Weckhuysen, Catalytic Dehydrogenation of Light Alkanes on Metals and Metal Oxides. *Chem. Rev.* **2014**, *114*, 10613–10653.

[15] M.S. Kumar, D. Chen, A. Holmen, J. C. Walmsley, Dehydrogenation of propane over Pt-SBA-15 and Pt-Sn-SBA-15: Effect of Sn on the dispersion of Pt and catalytic behavior. *Catal. Today* **2009**, *142*, 17–23.

[16] S. Furukawa, A. Tamura, K. Ozawa, T. Komatsu, Catalytic properties of Pt-based intermetallic compounds in dehydrogenation of cyclohexane and n-butane. *Appl. Catal. A Gen.* **2014**, *469*, 300–305.

[17] N. Kaylor, R. J. Davis, Propane dehydrogenation over supported Pt-Sn nanoparticles. *J. Catal.* **2018**, *367*, 181–193.

[18] H. N. Pham, J. J. H. B. Sattler, B. M. Weckhuysen, A. K. Datye, Role of Sn in the Regeneration of Pt/gamma-Al2O3 Light Alkane Dehydrogenation Catalysts. *ACS Catal.* **2016**, *6*, 2257–2264.

[19] A. Moscu, L. Veyre, C. Thieuleux, F. Meunier, Y. Schuurman, CO PROX over Pt-Sn/Al2O3: A combined kinetic and in situ DRIFTS study. *Catal. Today* **2015**, *258*, 241–246.

[20] W. D. Michalak, J. M. Krier, S. Alayoglu, J. Y. Shin, K. An, K. Komvopoulos, Z. Liu, G. A. Somorjai, CO oxidation on PtSn nanoparticle catalysts occurs at the interface of Pt and Sn oxide domains formed under reaction conditions. *J. Catal.* **2014**, *312*, 17–25.

[21] M. M. Schubert, M. J. Kahlich, G. Feldmeyer, M. Hüttner, S. Hackenberg, H. A. Gasteiger, R. J. Behm, Bimetallic PtSn catalyst for selective CO oxidation in H-2-rich gases at low temperatures. *Phys. Chem. Chem. Phys.* **2001**, *3*, 1123–1131.

[22] Y. J. Leng, X. Wang, I. M. Hsing, Assessment of CO-tolerance for different Pt-alloy

anode catalysts in a polymer electrolyte fuel cell using ac impedance spectroscopy. *J. Electroanal. Chem.* **2002**, *528*, 145–152.

[23] X. Wang, I. M. Hsing, Kinetics investigation of H-2/CO electro-oxidation on carbon supported Pt and its alloys using impedance based models. *J. Electroanal. Chem.* **2003**, *556*, 117–126.

[24] A. Moscu, Y. Schuurman, L. Veyre, C. Thieuleux, F. Meunier, Direct evidence by in situ IR CO monitoring of the formation and the surface segregation of a Pt-Sn alloy. *Chem. Commun.* **2014**, *50*, 8590–8592.

[25] O. Dulaurent, X. Courtois, V. Perrichon, D. Bianchi, Heats of adsorption of CO on a Cu/Al2O3 catalyst using FTIR spectroscopy at high temperatures and under adsorption equilibrium conditions. *J. Phys. Chem. B* **2000**, *104*, 6001–6011.

[26] M. Boualleg, D. Baudouin, J. M. Basset, F. Bayard, J. P. Candy, J. C. Jumas, L. Veyre, C. Thieuleux, Unexpected, spontaneous and selective formation of colloidal Pt3Sn nanoparticles using organometallic Pt and Sn complexes. *Chem. Commun.* **2010**, *46*, 4722–4724.

[27] A. Moscu, C. Theodoridi, L. Cardenas, C. Thieuleux, D. Motta-Meira, G. Agostini, Y. Schuurman, F. Meunier, CO dissociation on Pt-Sn nanoparticles triggers Sn oxidation and alloy segregation. *J. Catal.* **2018**, *359*, 76–81.

[28] J. Creuze, H. Guesmi, C. Mottet, B. Zhu, B. Legrand, Surface segregation in AuPd alloys: Ab initio analysis of the driving forces. *Surf. Sci.* **2015**, *639*, 48–53.

[29] B. Zhu, G. Thrimurthulu, L. Delannoy, C. Louis, C. Mottet, J. Creuze, B. Legrand, H. Guesmi, Evidence of Pd segregation and stabilization at edges of AuPd nano-clusters in the presence of CO: A combined DFT and DRIFTS study. *J. Catal.* **2013**, *308*, 272–281.

[30] B. Zhu, J. Creuze, C. Mottet, B. Legrand, H. Guesmi, CO Adsorption-Induced Surface Segregation and Formation of Pd Chains on AuPd(100) Alloy: Density Functional Theory Based Ising Model and Monte Carlo Simulations. *J. Phys. Chem. C*, **2016**, *120*, 350–359.

[31] M. Tsuda, H. Kasai, Ab initio study of alloying and straining effects on CO interaction with Pt. *Phys. Rev. B - Condens. Matter Mater. Phys.* **2006**, *73*, 155405.

[32] H. Li, M. Rivallan, F. Thibault-Starzyk, A. Travert, F. C. Meunier, Effective bulk and surface temperatures of the catalyst bed of FT-IR cells used for in situ and operando studies. *Phys. Chem. Chem. Phys.* **2013**, *15*, 7321–7327.

[33] J. Sirita, S. Phanichphant, F. C. Meunier, Quantitative analysis of adsorbate concentrations by diffuse reflectance FT-IR. *Anal. Chem.* **2007**, *79*, 3912–3918.

[34] A. Paredes-Nunez, I. Jbir, D. Bianchi, F. C. Meunier, Spectrum baseline artefacts and correction of gas-phase species signal during diffuse reflectance FT-IR analyses of catalysts at variable temperatures. *Appl. Catal. A Gen.* **2015**, *495*, 17–22.

[35] G. Kresse, J. Hafner, Abinitio molecular dynamics for liquid-metals. *Phys. Rev.* **1993**, *47*, 558–561.

[36] J. P. Perdew, Y. Wang, Accurate and simple analytic representation of the electron-gas correlation energy (vol 45, 13244, 1992). *Phys. Rev. B* **2018**, *98*, 244–249.

[37] P. E. Blöchl, O. Jepsen, O. K. Andersen, Improved tetrehedron method for Brillouin-zone integrations. *Phys. Rev. B* **1994**, *49*, 16223–16233.

[38] G. Kresse, D. Joubert, From ultrasoft pseudopotentials to the projector augmented-wave method. *Phys. Rev. B* **1999**, *59*, 11–19.

[39] S. Grimme, J. Antony, S. Ehrlich, H. Krieg, A consistent and accurate ab initio parametrization of density functional dispersion correction (DFT-D) for the 94 elements H-Pu. *J. Chem. Phys.* **2010**, *132*, 154104.

[40] B. Zhu, J. Meng, Y. Gao, Equilibrium Shape of Metal Nanoparticles under Reactive Gas Conditions. *J. Phys. Chem. C* **2017**, *121*, 5629–5634.

[41] C. Kittel, *Introduction to Solid State Physics*, Wiley, New York, **1996**.

[42] G.A.Busch, R.Kebn, Semiconducting Properties of Gray Tin. *Solid State Phys.* **1960**, *11*, 1–40.

[43] N. G. Hörmann, A. Gross, P. Kaghazchi, Semiconductor-metal transition induced by nanoscale stabilization. *Phys. Chem. Chem. Phys.* **2015**, *17*, 5569–5573.

[44] E. R. Jette, F. Foote, Precision determination of lattice constants. *J. Chem. Phys.* **1935**, *3*, 605–616.

[45] S. Sabet, P. Kaghazchi, Communication: Nanosize-induced restructuring of Sn nanoparticles. *J. Chem. Phys.* **2014**, *140*, 191102.

[46] M. Chen, Y. Han, T. W. Goh, R. Sun, R. V. Maligal-Ganesh, Y. Pei, C. K. Tsung, J. W. Evans, W. Huang, Kinetics, energetics, and size dependence of the transformation from Pt to ordered PtSn intermetallic nanoparticles. *Nanoscale* **2019**, *11*, 5336–5345.

[47] R. Ismail, R. L. Johnston, Investigation of the structures and chemical ordering of small Pd-Au clusters as a function of composition and potential parameterisation. *Phys. Chem. Chem. Phys.* **2010**, *12*, 8607.

[48] F. Pittaway, L. O. Paz-Borbón, R. L. Johnston, H. Arslan, R. Ferrando, C. Mottet, G. Barcaro, A. Fortunelli, Theoretical Studies of Palladium-Gold Nanoclusters: Pd-Au Clusters with up to 50 Atoms. *J. Phys. Chem. C* **2009**, *113*, 9141–9152.

[49] M. Vandichel, H. Grönbeck, A dimer path for CO dissociation on PtSn. *Catal. Sci. Technol.* **2019**, *9*, 695–701.

[50] A. Virnovskaia, S. Morandi, E. Rytter, G. Ghiotti, U. Olsbye, Characterization of Pt,Sn/Mg(Al)O catalysts for light alkane dehydrogenation by FT-IR Spectroscopy and catalytic measurements. *J. Phys. Chem. C* **2007**, *111*, 14732–14742.

[51] F. C. Meunier, R. Kdhir, N. Potrzebowska, N. Perret, M. Besson, Unravelling Platinum-Zirconia Interfacial Sites Using CO Adsorption. *Inorg. Chem.* **2019**, *58*, 8021–8029.

[52] B.E. Hayden, A.M. Bradshaw, The adsorption of CO on Pt(111) studied by infrared reflection-absorption spectroscopy. Surf. Sci. **1983**, *125*, 787–802.

[53] H. A. Aleksandrov, K. M. Neyman, K. I. Hadjiivanov, G. N. Vayssilov, Can the state of platinum species be unambiguously determined by the stretching frequency of an adsorbed CO probe molecule?. *Phys. Chem. Chem. Phys.* **2016**, *18*, 22108–22121.

[54] O. Dulaurent, D. Bianchi, Adsorption isobars for CO on a Pt/Al2O3 catalyst at high temperatures using FTIR spectroscopy: isosteric heat of adsorption and adsorption model. *Appl. Catal. A Gen.* **2000**, *196*, 271–280.

[55] L. Vitos, A. V. Ruban, H. L. Skriver, J. Kollár, The surface energy of metals. *Surf. Sci.* **1998**, *411*, 186–202.